

Retrieving the Hemodynamic Response Function in resting state fMRI: methodology and applications

Guo-Rong Wu^{a,b} and Daniele Marinazzo^a

a) Department of Data Analysis, Faculty of Psychology and Pedagogical Sciences, University of Ghent, Belgium
b) Key Laboratory of Cognition and Personality, Southwest University, Chongqing, China

Abstract

We present a procedure to retrieve the hemodynamic response function from resting state (RS) fMRI data. The fundamentals of the procedure are further validated by a simulation and with ASL data. We then present the modifications to the shape of the HRF at rest when opening and closing the eyes using a simultaneous EEG-fMRI dataset. Finally, the HRF variability is further validated on a test-retest dataset.

I. INTRODUCTION

Functional MRI time series can be modeled as the convolution of a latent neural signal (which is not measured) and the hemodynamic response function (HRF). First, since the temporal characteristics of the HRF across different anatomical regions can be influenced by the underlying venous structure, it is possible that intrinsic activity across disparate brain regions can be temporally correlated only due to the underlying vascular architecture. Second, the hemodynamic response is affected by physiological fluctuations arising from cardiac pulsation and respiration (Cordes, Haughton et al. 2001). These can introduce temporal correlations in fMRI signals. Also, given the fact that fMRI data is sampled slowly (typically every 1-2 seconds), physiological fluctuations cannot be removed by simple filtering as they can alias into the low frequency band of interest (0.01-0.1 Hz). Third, the period of the fastest

variation in RS-fMRI data is 10 s, which is orders of magnitude greater than the sub-second time scale at which most neuronal processes occur.

This confounding effect can be dealt with by deconvolution of the HRF. In task-related fMRI this procedure has been known and applied since the very beginnings, since the onset of the HRF was known. This is not the case for RS-fMRI.

Motivated by this evidence, we developed an approach to perform blind hemodynamic deconvolution (Wu, Liao et al. 2013) of RS-fMRI data to recover the underlying latent neuronal signals. This allowed to greatly improve the estimation of directed dynamical influences in RS-fMRI recordings (Wu, Liao et al. 2013), but also provided us with an estimation of the HRF shape for each voxel in the brain. In this chapter we will first validate the blind HRF retrieving approach by means of a simulation and a comparison with baseline CBF, then we will analyze the effects of physiological conditions (eyes open vs. eyes closed) on the HRF shape; finally the HRF variability will be assessed with the help of a test-retest resting state fMRI dataset.

II. METHODOLOGY

The deconvolution is blind because there is no external input in case of RS-fMRI data and consequently, both the HRF and the underlying neuronal latent variables must be simultaneously estimated from the observed fMRI data, making this an ill-posed estimation problem.

We will now briefly review the foundations of a blind HRF retrieval technique for resting-state BOLD-fMRI signal developed in a previous work (Wu, Liao et al. 2013).

There is accumulated evidence of specific BOLD events governing the dynamics of the brain at rest (Tagliazucchi, Balenzuela et al. 2012, Petridou, Gaudes et al. 2013). We start from the assumption that resting-state brain dynamics can be driven by spontaneous events, which can be seen as a point process. A linear time invariant (LTI) system is used to model the relationship between the spontaneous neural

event and the BOLD response. The hemodynamic response $h(t)$ represents such dynamic process; the BOLD signal at time t , $y(t)$, is modeled as the convolution of neural state $x(t)$ and $h(t)$, i.e.

$$y(t) = s(t) \otimes h(t) + \varepsilon(t).$$

where \otimes denotes convolution, and $\varepsilon(t)$ is the unexplained error.

The right side of the above equation includes three unobserved quantities. In order to solve the equation for $h(t)$ we need to substitute $s(t)$ with a hypothetical model of the neural activation for $s(t)$. Here we employ a stimulus function $\hat{s}(t)$ to model $s(t)$. $\hat{s}(t)$ is constituted by several time-shifted delta functions, which are centered at the onset of each spontaneous point process events. For task-related fMRI, the stimulus function is always derived according to the prior task design information. This is not the case for resting state fMRI. We need to retrieve the spontaneous point process event from a given signature (spike/peak) in the BOLD time series. As the peak of the BOLD signal lags behind the peak of neural activation (i.e. k seconds), it is reasonable to assume that these BOLD spikes are generated from the spontaneous point process events.

In order to obtain the time lag k , we search all values in the interval $[0, \text{PST}]$, where PST is the peristimulus time, choosing the one for which the noise squared error (i.e. $|y(t) - \hat{s}(t) \otimes h(t)|^2$) is smallest, indicating the spontaneous event onset. In practice, The timing set s of these resting-state BOLD spikes/transients is defined as the time points exceeding a given threshold μ around a local peak, which can be detected according to the following expression:

$$S\{i\} = t^i, y(t^i) \geq \mu \text{ & } y(t^i) \geq y(t^i - \tau) \& y(t^i) \geq y(t^i + \tau).$$

It is worth mentioning that we make no assumptions about the exact shape or functional form of the hemodynamic responses. The application of prior knowledge about possible hemodynamic response shapes could reduce the bias in the linear estimation framework especially for the low signal noise ratio dataset, and sharply

reduce the computational cost. Therefore, we assume that the hemodynamic responses for all resting state spontaneous point process events and at all locations in the brain are fully contained in an d -dimensional linear sub-space H of \Re^d , then, any hemodynamic response h can be represented uniquely as the linear combination of the corresponding basis vectors. The canonical HRF with its delay and dispersion derivatives (we denote it as canon2dd) are employed as the basis functions in our previous study (Wu, Liao et al. 2013). The HRF can also be reconstructed via (smoothed) Finite Impulse Response (sFIR) or ‘selective averaging’ (Dale and Buckner 1997).

There are some implicit limitations in our previous work described so far.

- (1) $\varepsilon(t) \sim N(0, \sigma_1^2)$ is assumed to be white. However, $\varepsilon(t)$ is not independent in time due to aliased biorhythms and neural activity not accounted for in the model.
- (2) The spontaneous point process event onsets need to be synchronized with scans, i.e. the time lag k is an integral multiple of TR, which may induce some bias.
- (3) in equation 1, the baseline activity is not included.

To reduce the above estimation bias, we modify the algorithm to account for the temporal dependency in $\varepsilon(t)$, and the mismatching between events onset and scans, in the following way:

- (1) Using an AR(p) model during the parameter estimation of temporal correlation structure in $\varepsilon(t)$.
- (2) Estimating the time lag in a much finer temporal grid rather than TR, i.e. the peak of BOLD response lags behind the peak of neural activation is presumed to $k \times TR / N$ seconds (where $0 < k < PST \times N / TR$).
- (3) Adding a constant term into equation 1,

$$y(t) = s(t) \otimes h(t) + c + \varepsilon(t) \quad (2)$$

where c indicates the baseline magnitude of the BOLD response.

To characterize the shape of the hemodynamic response, three parameters of the HRF, namely response height and its normalization (normalized by baseline magnitude c , i.e. percent signal change, PSC), time to peak, Full Width at Half Maximum (FWHM), were estimated. These quantities are interpretable in terms of potential proxies for response magnitude, latency and duration of neuronal activity (Lindquist and Wager 2007).

The procedure described above is sketched in Figure 1.

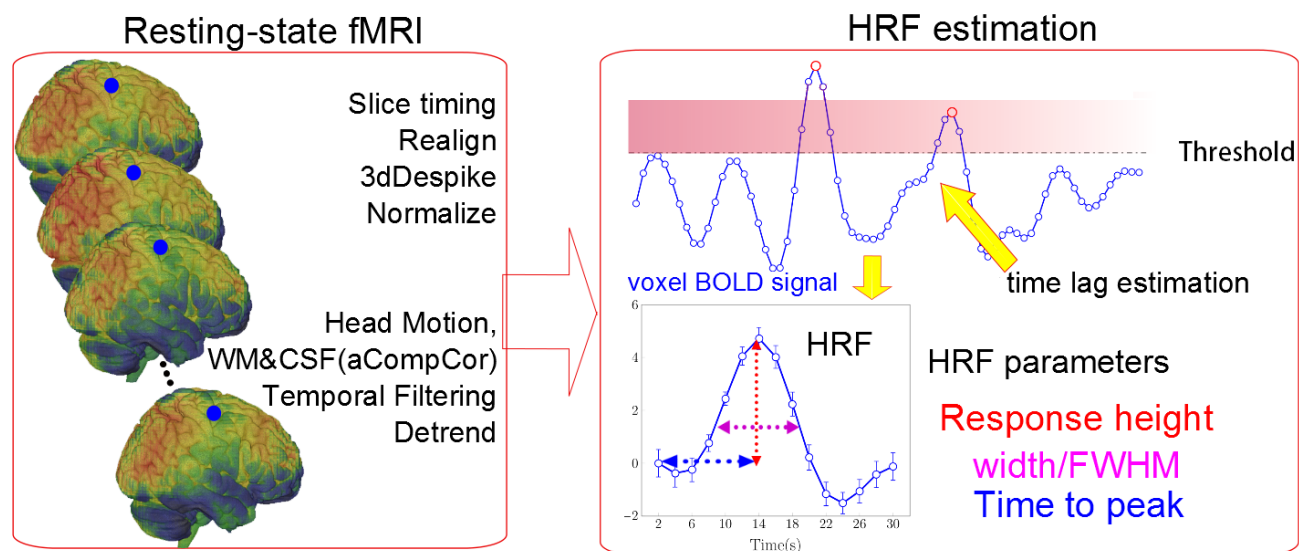


Figure 1: scheme of the resting state HRF retrieving procedure.

III. APPLICATIONS AND DISCUSSION

1. Simulation

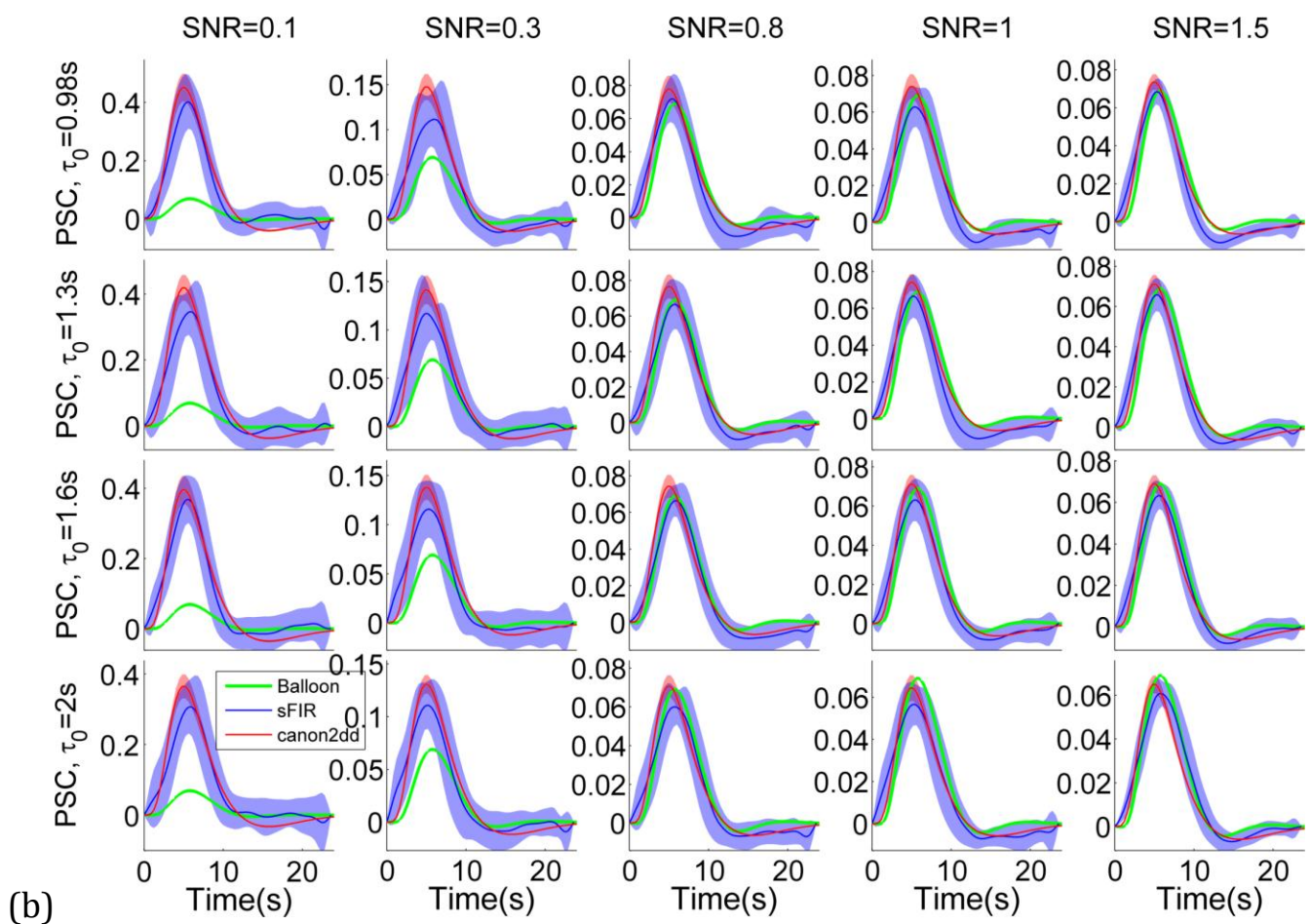
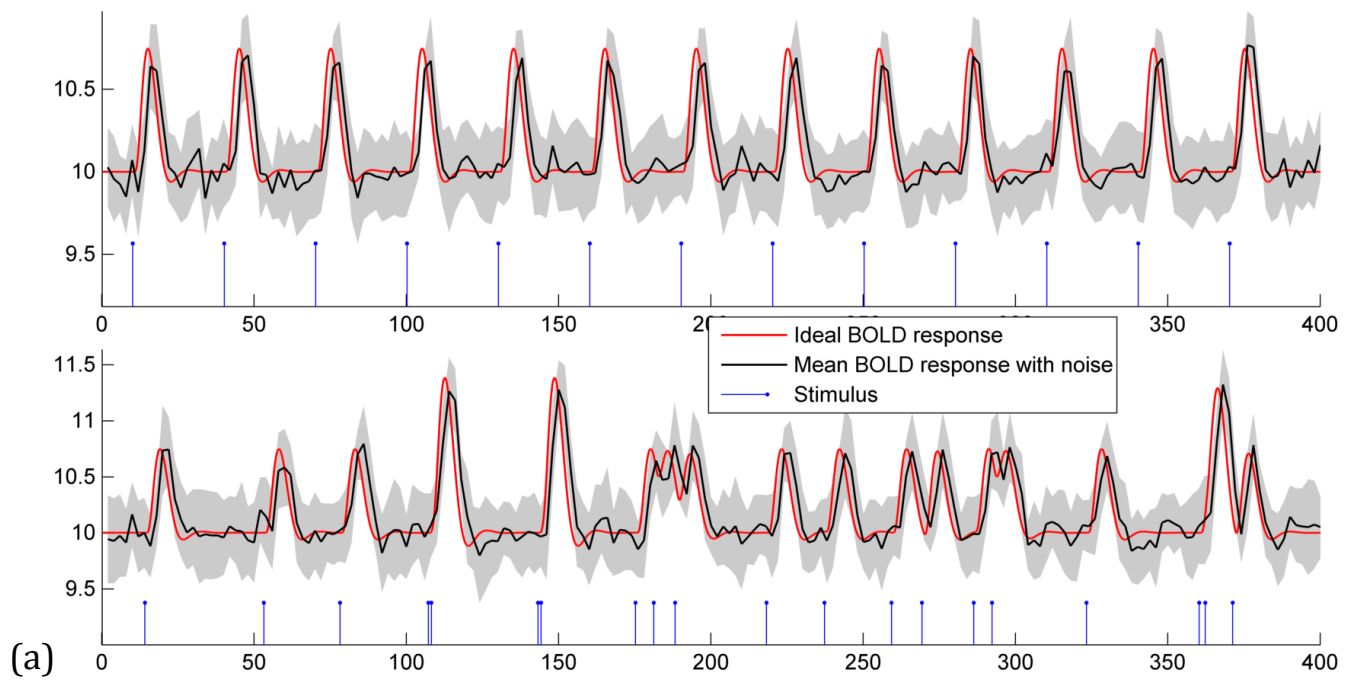
To validate the feasibility and effectiveness of proposed algorithm, the simulated HRFs are used as the ground truth for simulations. The HRF was generated using a physiological model, the balloon model (Buxton, Wong et al. 1998), with TR=2s and the parameters used SPM package: signal delay = 0.64, autoregulation= 0.32, exponent for $F_{out}(v)$ = 0.32, resting oxygen extraction = 0.4, and varying transit time (τ_0) = 0.98, 1.3, 1.6, 2. The transit time is V_0/F_0 , where V_0 is resting blood volume fraction and F_0 is resting flow. The physiology of the relationship between

flow and volume is determined by the evolution of the transit time (Friston, Mechelli et al. 2000). Two types of stimulus designs are employed to simulate the BOLD signal:

1. Event-related (ER) design (0.1s on) with fixed inter-stimulus-interval (ISI) of 40 s,
2. Jittered ER design with non-uniform ISI (average ISI = 19s).

Different levels of white noise ϵ , modeled by an autoregressive AR(1) process with AR coefficient of 0.2, are added such that the resulting SNR ($\sigma_{Signal}/\sigma_{Noise}$, where s is the standard deviation) are 1.5 (low noise) and 0.1 (high noise). Each ER design simulation is run 20 times with random values of ϵ in order to generate a null distribution (in order to ensure reliability of the result and calculate the mean and standard deviation of the HRF).

We observe that the retrieved HRF shapes are dependent on the SNR. As expected, the variability of canon2dd HRF is much lower than sFIR model across all level of SNR, both for fixed and non-uniform ISI. As shown in Figure 2, two HRF basis vectors show similar but different degree of fitting of ground truth HRF, slightly vary with different transit time. These stable characteristics implicate that the proposed algorithm could be a robust indicator of spontaneous BOLD response. Besides, as the balloon model is a nonlinear HRF model, the jittered design may induce nonlinear interaction between stimuli, which could violate the assumption behind the proposed algorithm (Boynton, Engel et al. 2012).



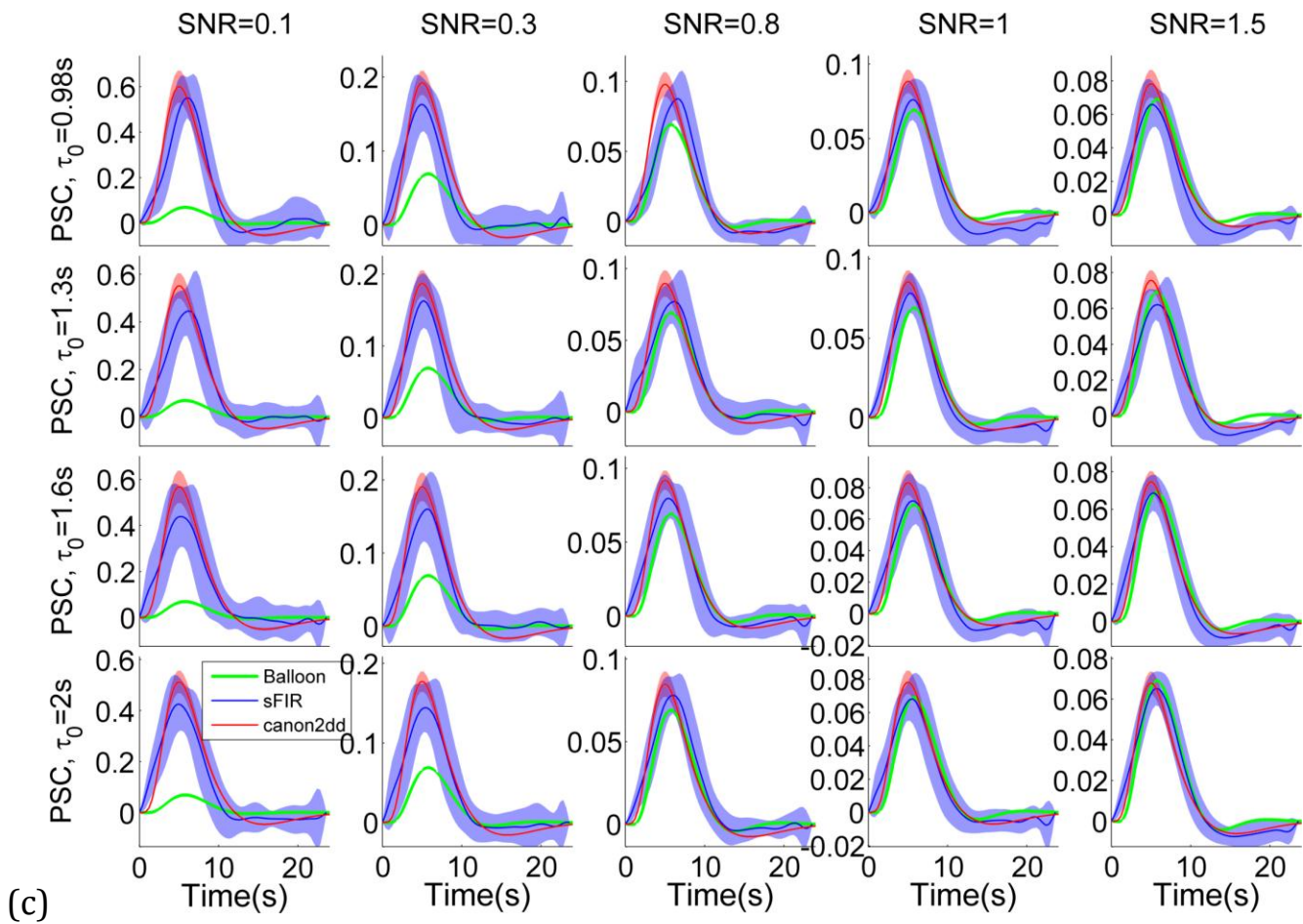


Figure 2 shows (a) ER stimulus timing, the ideal BOLD response, and ideal response corrupted with noise (SNR=1) (b) Ground truth (Balloon) and estimated HRFs for fixed ISI ER design, (c) Ground truth and estimated HRFs for jittered ER design. The colored shadow indicates the standard deviation.

2. Relation with cerebral blood flow

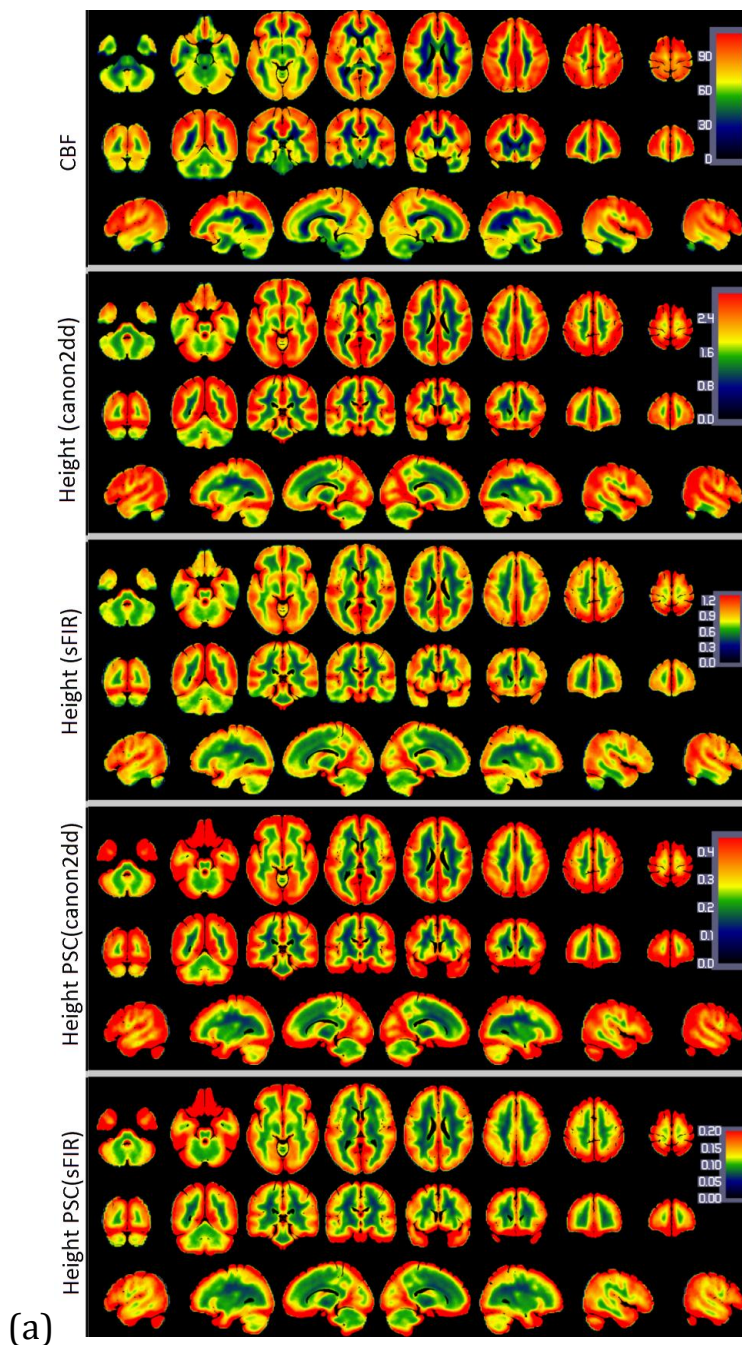
The BOLD-fMRI signal reflects the complex interactions between cerebral metabolic rate of oxygen, cerebral blood flow (CBF) and volume; the comparison of CBF and HRF in the same voxels could provide a better understanding of the temporal dynamics of resting state spontaneous responses. In this section we employ a public dataset (Avants, Duda et al. 2015) to explore the relationship between baseline CBF and HRF.

The resting state BOLD fMRI images were acquired using 2D EPI sequence (TR=2s, 8 min). Subjects (N=108, some of them with longitudinal data) were required to relax

quietly while looking at a fixation point. Pseudo continuous arterial spin labeled (pCASL) images were acquired using gradient-EPI with TR/TE=4,000/12 ms. The total imaging time was 5.5 min, and 40 label/control pairs were acquired, with 1.5 s labeling duration and 1.2 s post-labeling delay.

BOLD fMRI images were preprocessed with SPM12, including: realigning and unwarping, coregistration to anatomical image, spatial normalization into MNI space, smoothing, detrending, and linear regression to remove possible spurious variances from the data (including six head motion parameters, non-neuronal sources of noise estimated using the anatomical component correction method, i.e. white matter and cerebral spinal fluid signal), 0.008~0.1HZ band filtering. As the slice order information is not reported in this dataset, we did not perform the slice timing correction, which does not affect the HRF retrieving algorithm anyway. pCASL data were preprocessed using the ASLtbx toolbox (Wang, Aguirre et al. 2008), with the following steps: realigning, coregistration to anatomical image, regression of the six head motion parameters and smoothing with 6mm FWHM Gaussian kernel. CBF was then estimated, and finally normalization to MNI space was performed (same normalization method used in BOLD fMRI images). The group median map of CBF and HRF parameters are presented in Figure 3. We can observe that the HRF response height shows a spatial pattern similar to the CBF map. A prior functional parcellation of cerebrum is applied on the median map to validate the effect of spatial correlations between them. The prior functional parcellation is composed of seven large-scale subnetworks: visual (VN), somatomotor (SMN), dorsal attention (DAN), ventral attention (VAN), limbic (LN), frontoparietal (FPN) and default network (DMN) (Yeo, Krienen et al. 2011). The correlation analysis across voxels in each subnetworks showed a striking spatial overlap between CBF and HRF response height (PSC, baseline) (Figure 4). Such phenomenon is not observed in other HRF parameters. In particular there is evidence of a highly nonlinear relationship between height PSC/baseline and CBF. In the DMN (baseline)

and LN (height PSC) the linear relation is not evident, both for canon2dd and sFIR model. Furthermore, the across subject correlation between CBF and HRF were also analyzed both at voxel level and large-scale networks level (Figure 5 & 6). We found different HRF model show different correlation with CBF at the both spatial resolutions. In contrast to canon2dd, sFIR show higher correlation in HRF response height, lower in time to peak. The physiological basis of this complicated interaction will need to be investigated further.



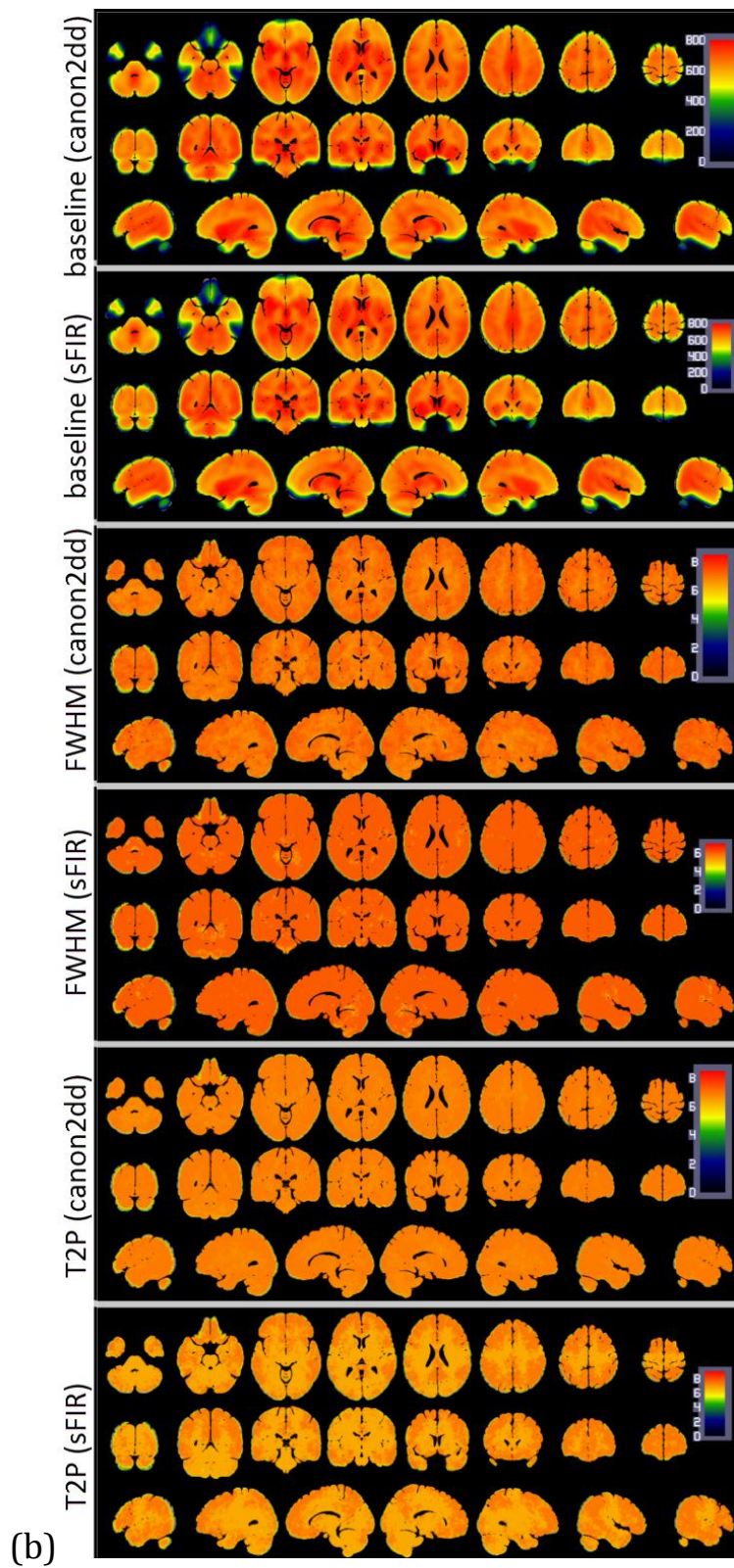


Figure 3. Median maps of CBF (a) and HRF (b) parameters across subjects.

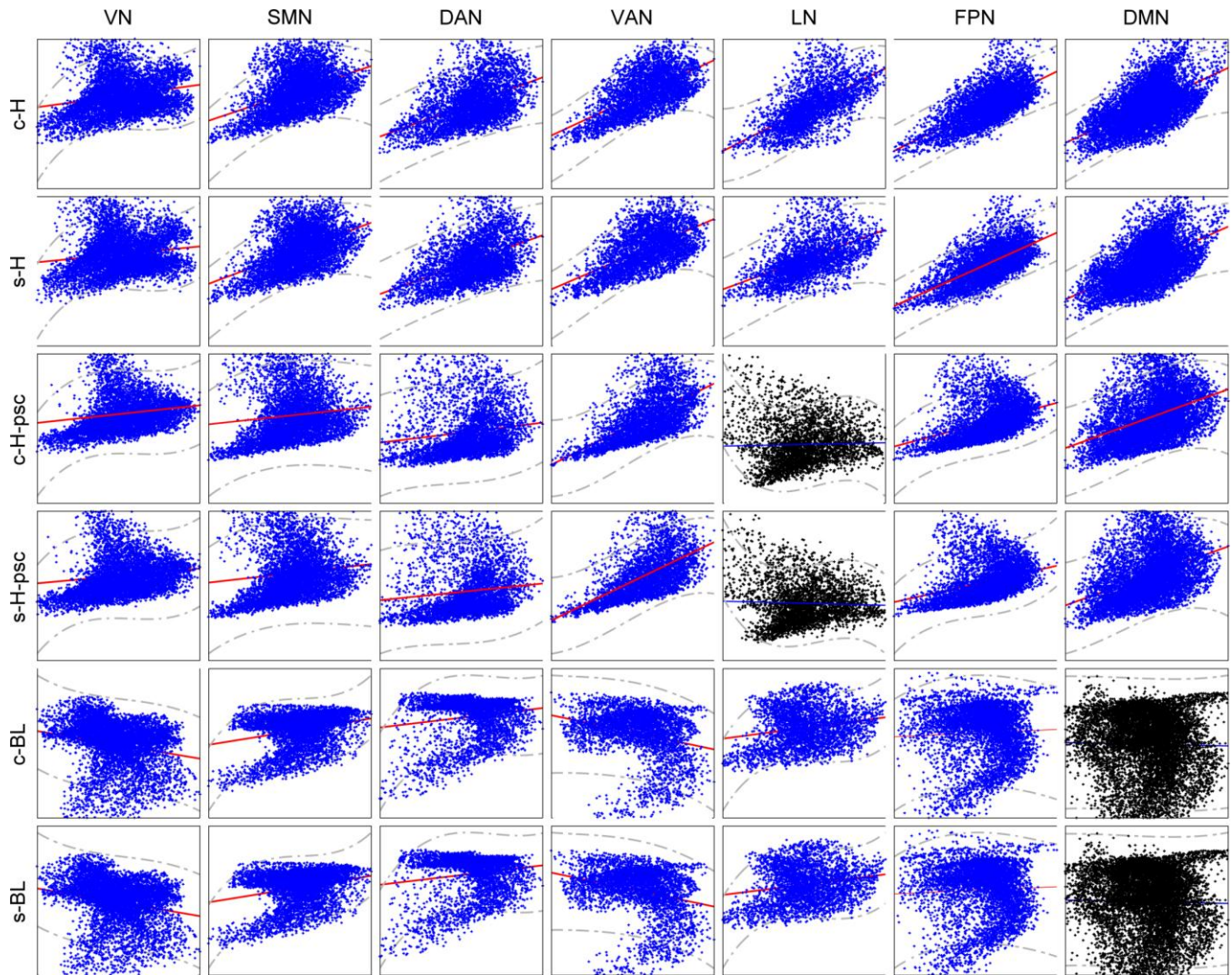


Figure 4. Scatterplot of the spatial correlations across voxels between CBF and HRF parameters. The X-axis is the CBF, Y-axis are the HRF parameters. Blue scatterplots indicate that the linear correlation is significant, $p < 0.05$, corrected.

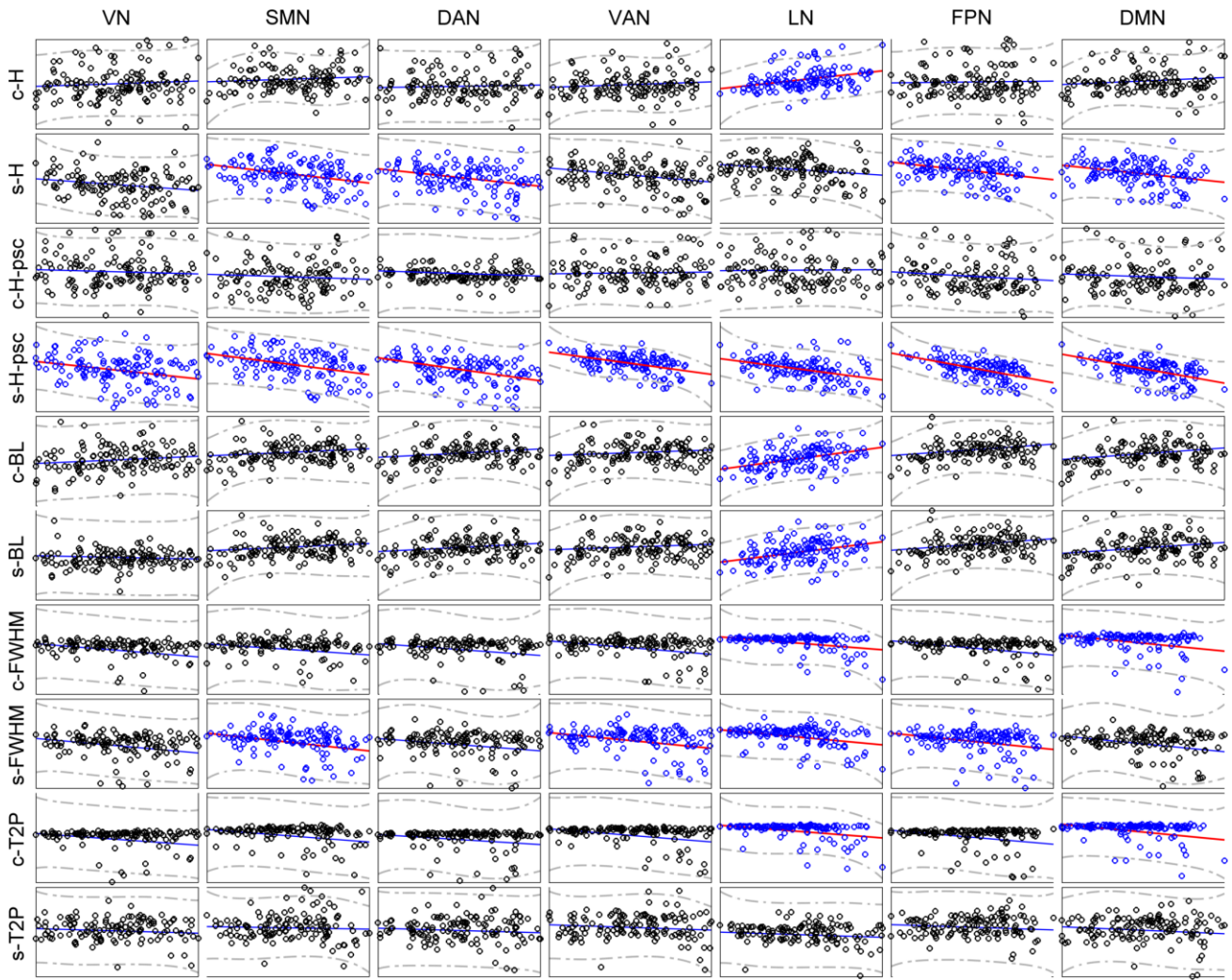


Figure 5. Scatterplot of the across subject correlations between CBF and HRF parameters. X-axis is the CBF, Y-axis are the HRF parameters. Blue scatterplots indicate the linear correlation is significant, $p < 0.05$, corrected.

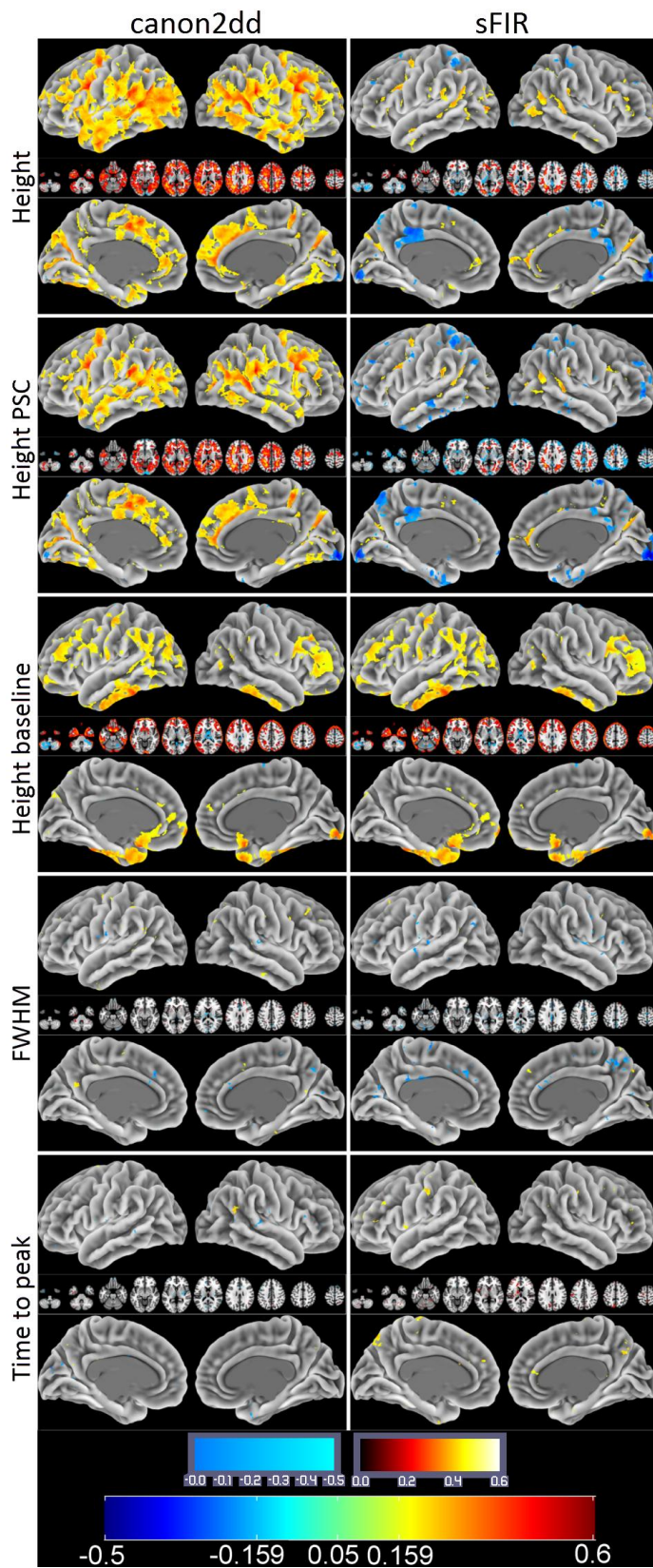


Figure 6. Correlations between CBF and HRF parameters at voxel level across subjects. The upper colorbar is for inside plots, the bottom colorbar is for surface plots.

3.Relation with EEG power

In order to further investigate the electrophysiological basis of the HRF and its coupling to electrical brain activity we considered simultaneously recorded EEG and fMRI data. EEG were collected at 1000 Hz and down-sampled at 250 Hz. Scanner artifact correction, pulse artifact correction, notch filtering and ICA analysis were performed on the raw data. fMRI data were collected at 7 Tesla, with a repetition time of 1s. Resting-state fMRI data preprocessing was carried out using both AFNI and SPM8 package. First, the EPI volumes were corrected for the temporal difference in acquisition among different slices, and then the images were realigned to the first volume for head-motion correction. The resulting volumes were then despiked using AFNI's 3dDespike algorithm to mitigate the impact of outliers. Next, the despiked images were spatially normalized to the Montreal Neurological Institute template then resampled to 3-mm isotropic voxels.

Several parameters were included in a linear regression to remove possible spurious variances from the data. These were i) six head motion parameters obtained in the realigning step, ii) non-neuronal sources of noise estimated using the anatomical component correction method (aCompCor, the representative signals of no interest from white matter (WM) and cerebral spinal fluid (CSF) included the top five principal components (PCs) from WM and the top five from CSF mask; the subject-specific WM and CSF masks was segmented from the anatomical image of each participant using SPM8's unified segmentation-normalization procedure) (Behzadi, Restom et al. 2007). Then the time series were temporally band-pass filtered (0.01~0.08 Hz) and linearly detrended.

The scalp EEG voltage data from the three occipital channels O1, O2, and Oz were selected (Mo, Liu et al. 2013).

First, EEG signals for each channel were segmented into 500 ms non-overlapping epochs. Second, the EEG power spectrum for each single epoch was calculated using a nonparametric multitaper approach, and the alpha band power was obtained by integrating the power spectrum between 8 and 12 Hz. Third, the channel-level alpha power time series from each of the three occipital channels was averaged to yield the subject-level alpha power time series, which was convolved with a canonical hemodynamic response function (HRF). The HRF-convolved alpha power time series was then downsampled to the same sampling frequency as the BOLD signal.

To identify brain regions whose BOLD activity co-varied with EEG alpha power, we examined the temporal correlation between HRF-convolved alpha power time series and BOLD time series from all voxels based on the general linear model (GLM). HRF-convolved alpha power time series was incorporated as a parametric regressor in the GLM, modeling the coupling effects between alpha and BOLD.

The processed BOLD signal at every voxel was converted into its z-score, and the resting state HRF was retrieved as described above, according to the canon2dd and sFIR model.

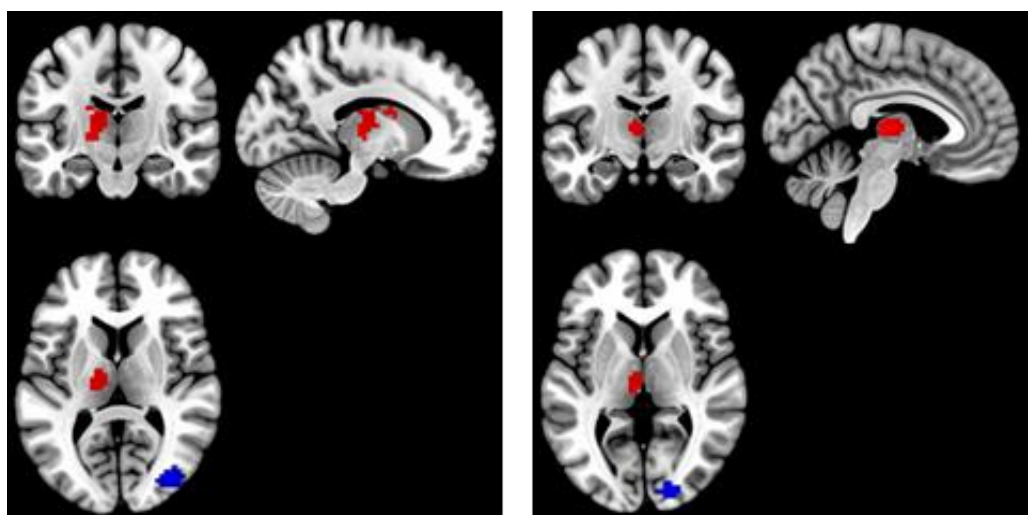


Figure 7: clusters of significant correlation (red) and anti-correlation (blue) between BOLD and alpha power spectrum

Two canonical ROIs were chosen from the previous GLM analysis (Thalamus and Occipital Lobe) (Laufs, Kleinschmidt et al. 2003), both for eye closed and open condition, under individual voxel p-value $<10^{-6}$, cluster size >50 .

A positive correlation between BOLD and canonical HRF convolved alpha power was observed in the thalamus, and a negative one in the Occipital Lobe (Figure 7). After (canon2dd and sFIR) HRF deconvolution, the Pearson correlation between devonvolved BOLD and alpha power is almost strengthened, only one weaken connectivity is found in thalamus with eye closed after canon2dd HRF deconvolution (Figure 8).

The voxel-level HRF shapes derived in these two regions in the two conditions are reported in Figure 9. We observe opposite patterns of HRF shapes between the thalamus and occipital cortex under the two conditions, which is consistent with the correlation and anti-correlation between the alpha power spectrum and BOLD signal in thalamic and occipital cortex. It is worth to note how the variations in HRF are consistent with the differences in net arterial and venous flow, and the consequent effects on the estimation of Granger causality reported in (Webb, Ferguson et al. 2013). This evidence confirms the importance of performing HRF deconvolution prior to estimating not only for lag-based directed connectivity (Wu, Liao et al. 2013), but also for standard functional connectivity .

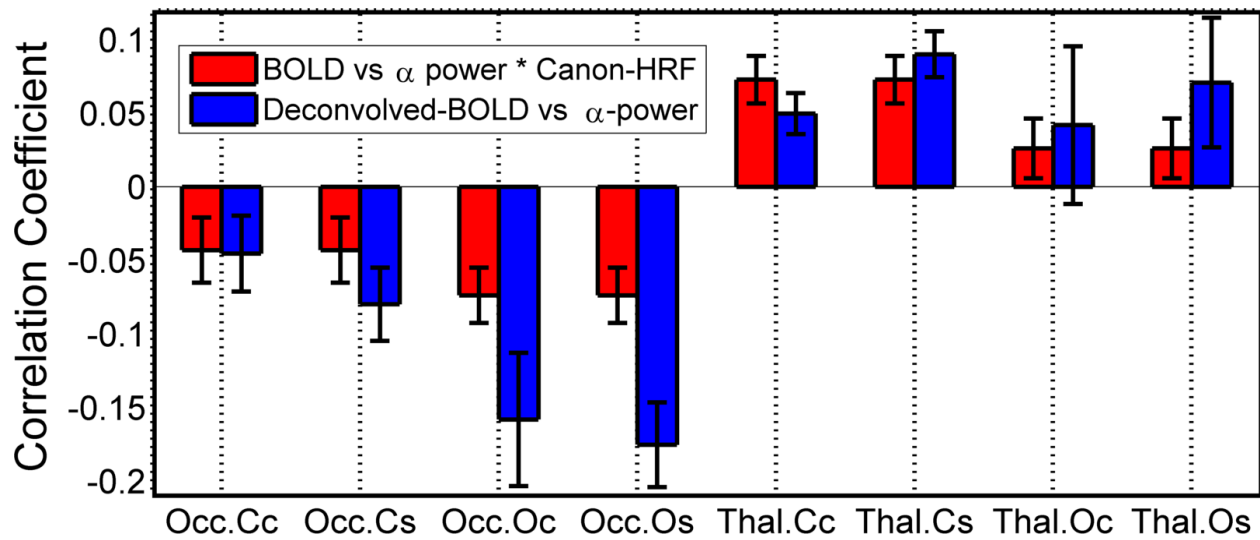


Figure 8. Pearson correlation between (BOLD) Deconvolved BOLD signal and (canonical HRF convolved) alpha power. Occ: occipital area; Thal: thalamus; Cc: eyes closed, canon2dd; Cs: eyes closed, sFIR; Oc: eyes open, canon2dd; Os: eyes open, sFIR.ss

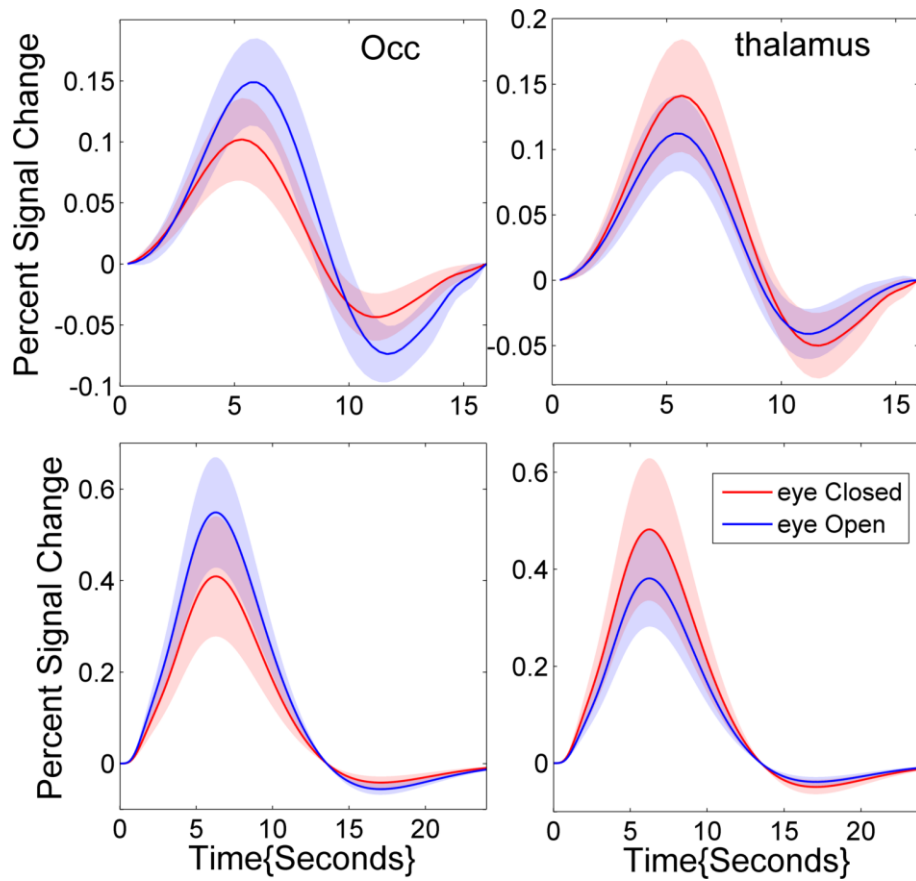


Figure 9: HRF at rest in the occipital cortex (left) and in the thalamus (right) for eyes open and closed. Left upper pannel is HRF estimated by sFIR model, the bottom pannel

is HRF estimated by canonical HRF with its derivatives. The red and blue shadows are the standard deviations of voxelwise HRFs under eyes closed and open conditions.

4. HRF modulations with eyes open and closed

In order to study the modulations of HRF shape when opening or closing the eyes on a larger sample, we considered a dataset of 48 healthy controls collected at the Beijing Normal University in China with 3 resting state fMRI scans of six minutes each (http://fcon_1000.projects.nitrc.org/indi/IndiPro.html). During the first scan participants were instructed to rest with their eyes closed. The second and third resting state scan were randomized between resting with eyes open versus eyes closed. Data were preprocessed as described in above section. Then the resting state HRF was retrieved. Statistical significance of the spontaneous hemodynamic response evoked by opening and closing eyes was assessed with a group-level repeated-measures analysis of covariance (ANCOVA) that included subjects as the random factor and two fixed factors, resting state type (eyes closed and open) and order (eyes closed-open-closed, eyes closed-closed-open), age, gender, and mean FD power as the covariates. The ANCOVA revealed significant main effect for resting state type in hemodynamic response height. No significant main effect of order and interaction effect were found. The significant differences in the height of the HRF located in the occipital areas, and were depicted in figure 10. The corresponding HRF shape is also reported. Though the difference in the thalamus is not obvious, we still can find the opposite patterns of HRF shapes under eye closed and open, similar with the finding in EEG-fMRI dataset.

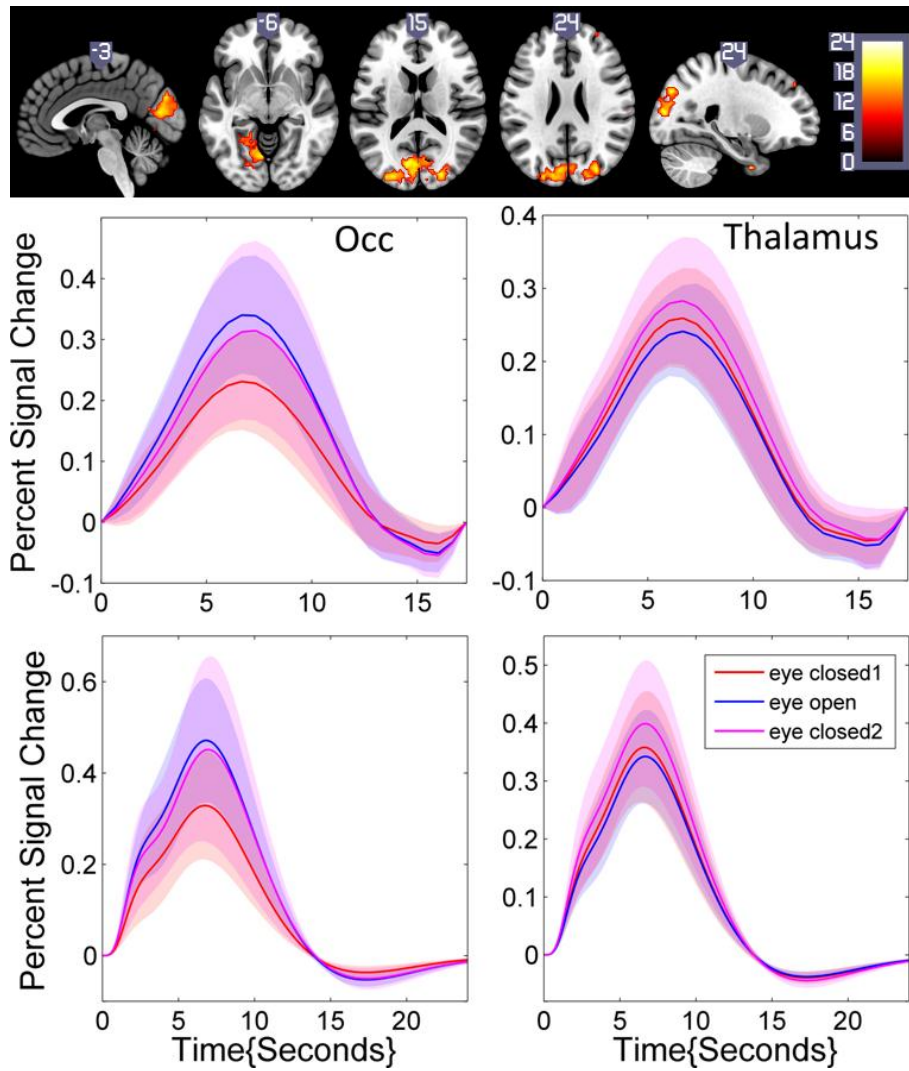


Figure 10: statistical differences in HRF height with eyes closed (1), open, then closed again (2) (top), and typical shapes in the occipital (left) and thalamic (right) area (middle: sFIR; bottom: canonical HRF with its derivatives).

5. HRF variability

The hemodynamic response has been shown to vary in timing, amplitude, and shape across brain regions and cognitive task paradigms (Miezin, Maccotta et al. 2000, Handwerker, Gonzalez-Castillo et al. 2012). Such variation is expected also for resting state. In order to investigate the variability on the resting state HRF, a test-retest reliability analyses were performed on a resting-state fMRI dataset that has been publicly released in the “1000 Functional Connectomes Project”. All included participants had no history of neurological and psychiatric disorders and

all gave the informed consent approved by local Institutional Review Board. During the scanning participants were instructed to keep their eyes closed, not to think of anything in particular, and to avoid falling asleep.

Two data sets with different TR (TR = 2.5 s and TR = 0.645 s) were acquired on Siemens 3T Trio Tim scanners using standard EPI sequence (TR = 2500msec, 3mm isotropic voxels, 5 minutes) and multiband EPI sequence (TR = 0.645 s, 3 mm isotropic voxels, 10 min).

To evaluate the test-retest (TRT) reliability of the voxel HRF parameters between the two sessions, a measurement of the intraclass correlation coefficient (ICC) was employed. A one-way ANOVA with random subject effects was used to compute the between-subject mean square (BMS) and within-subject mean square (WMS). Then an ICC value was subsequently calculated according to the equation (Shrout and Fleiss 1979)

$$ICC = \frac{BMS - WMS}{BMS + (m-1)WMS}$$

where m represents the number of repeated measurements of the voxel HRF parameter (here, $m = 2$). We calculated the ICC value for each voxel and generated the ICC map for each HRF parameter. Next, the TRT reliability of the HRF parameter was assessed in a voxel-wise manner with the classifying criteria of ICC values (Sampat, Whitman et al. 2006): less than 0.4 indicated low reliability; 0.4 to 0.6 indicated fair reliability; 0.6 to 0.75 indicated good reliability and 0.75 to 1.0 indicated excellent reliability. To further assess the regional variability of TRT reliability, we utilized the above-mentioned prior functional parcellation of cerebrum, and calculated the mean ICC values and their standard deviations within these subnetworks, respectively. As was expected, sFIR showed lower ICC than canon2dd model, both at voxel level and large-scale network level. We did not observe an obvious spatial pattern in the ICC maps for distinct networks. The hemodynamic response height (psc) showed good reliability for canon2dd model

acorss all subnetworks and TR (excluding the VN at TR=2.5s), and for sFIR in VAN, FPN and DMN at TR=2.5s, and fair reliability for most of the subnetworks with sFIR model. The other HRF parameters (FWHM and time to peak) showed low reliability. These results reveal that the different hemodynamic response sampling (i.e. in units of TR) only slightly affects the ICC maps of hemodynamic response height.

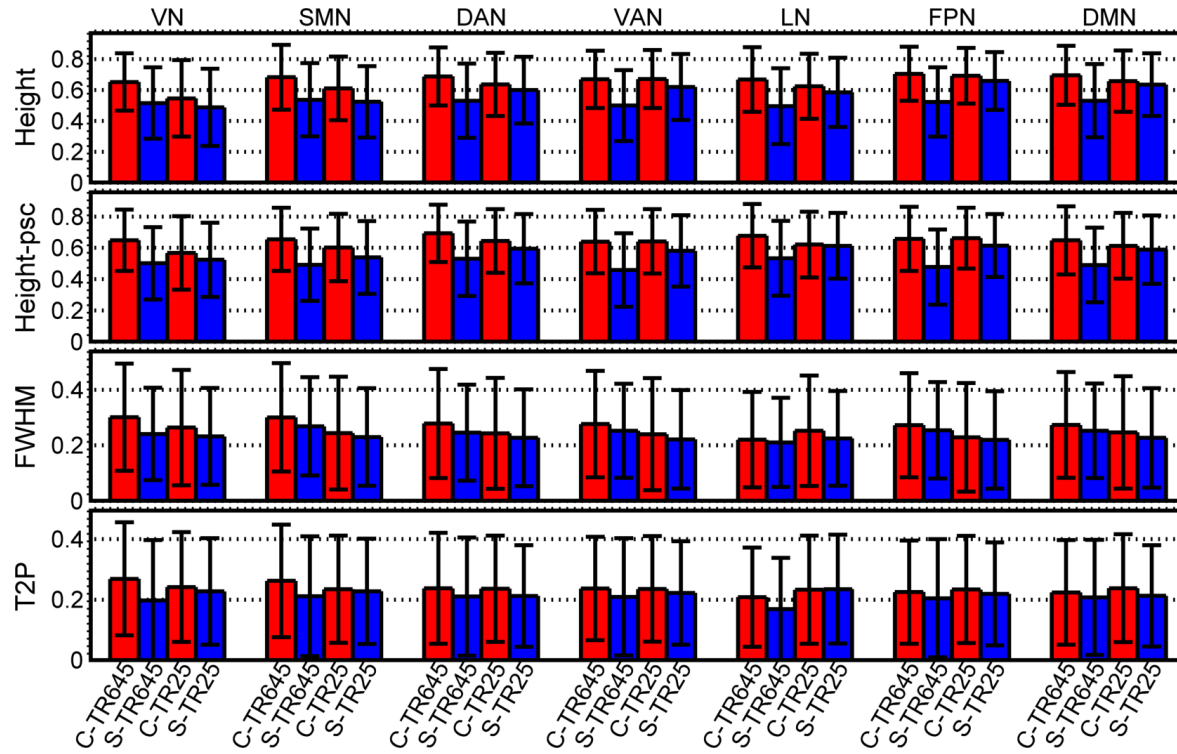


Figure 11. TRT reliability of HRF parameters within seven subnetworks. C-TR645: canon2dd HRF, TR=0.645s; S-TR645: sFIR HRF, TR=0.645s; C-TR25: canon2dd HRF, TR=2.5s; S-TR25: sFIR HRF, TR=2.5s; T2P: Time to peak.

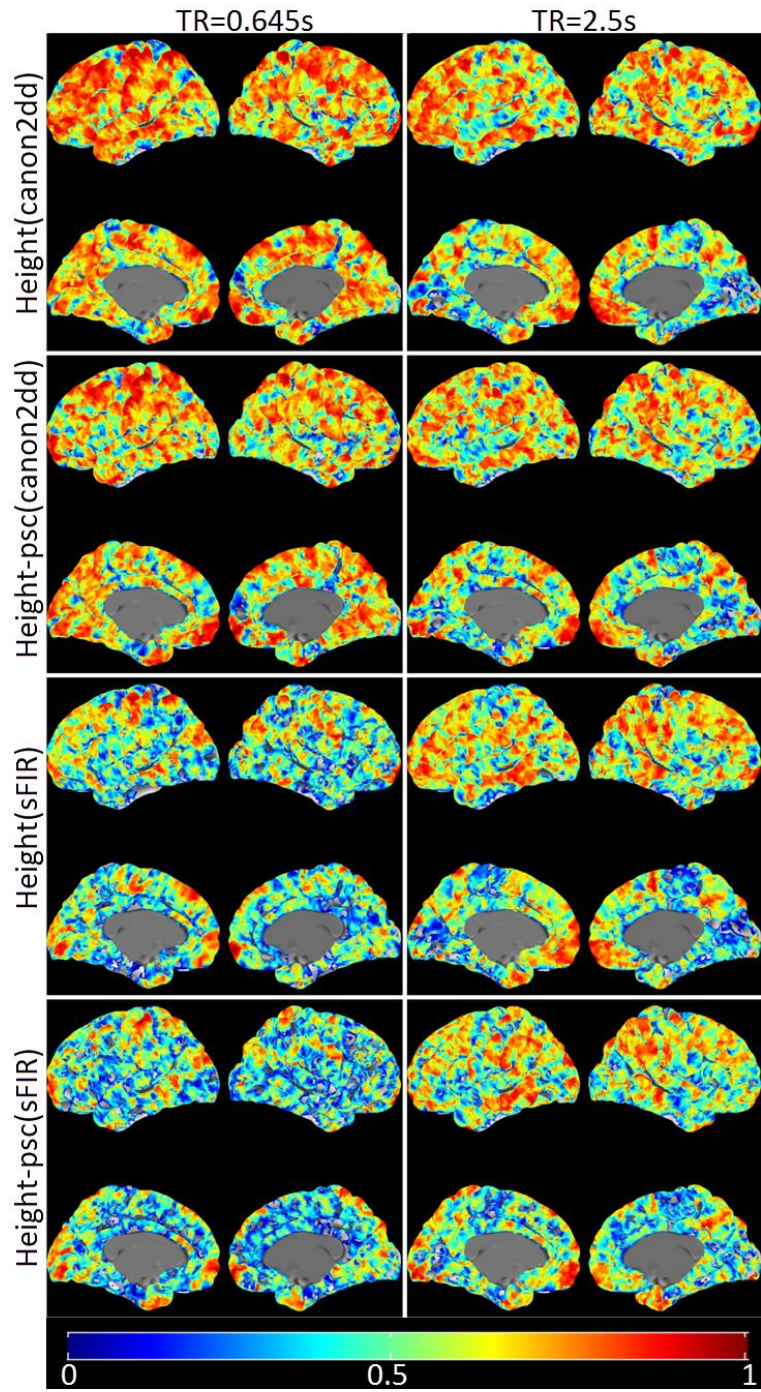


Figure 12. TRT reliability maps of hemodynamic response height (PSC) with different HRF basis vectors (canon2dd, sFIR), at different TR (0.645s, 2.5s).

IV. CONCLUSIONS AND FUTURE WORK

We have presented a methodology to retrieve the hemodynamic response function from resting state fMRI data. The feasibility and effectiveness of proposed algorithm is confirmed by simulation data. The results are promising since the retrieved HRF is consistent with the literature and supports evidences of the vascular flow. Additionally, functional modifications to the HRF shape are consistent with evidence previously reported using different methodologies. The approach will need further validation using electrophysiological and cardiovascular data.

REFERENCES

- Avants, B. B., J. T. Duda, E. Kilroy, K. Krasileva, K. Jann, B. T. Kandel, N. J. Tustison, L. Yan, M. Jog, R. Smith, Y. Wang, M. Dapretto and D. J. Wang (2015). "The pediatric template of brain perfusion." *Sci Data* **2**: 150003.
- Behzadi, Y., K. Restom, J. Liau and T. T. Liu (2007). "A component based noise correction method (CompCor) for BOLD and perfusion based fMRI." *Neuroimage* **37**(1): 90-101.
- Boynton, G. M., S. A. Engel and D. J. Heeger (2012). "Linear systems analysis of the fMRI signal." *Neuroimage* **62**(2): 975-984.
- Buxton, R. B., E. C. Wong and L. R. Frank (1998). "Dynamics of blood flow and oxygenation changes during brain activation: the balloon model." *Magn Reson Med* **39**(6): 855-864.
- Cordes, D., V. M. Haughton, K. Arfanakis, J. D. Carew, P. A. Turski, C. H. Moritz, M. A. Quigley and M. E. Meyerand (2001). "Frequencies contributing to functional connectivity in the cerebral cortex in "resting-state" data." *AJNR Am J Neuroradiol* **22**(7): 1326-1333.
- Dale, A. M. and R. L. Buckner (1997). "Selective averaging of rapidly presented individual trials using fMRI." *Hum Brain Mapp* **5**(5): 329-340.

- Friston, K. J., A. Mechelli, R. Turner and C. J. Price (2000). "Nonlinear responses in fMRI: the Balloon model, Volterra kernels, and other hemodynamics." *Neuroimage* **12**(4): 466-477.
- Handwerker, D. A., J. Gonzalez-Castillo, M. D'Esposito and P. A. Bandettini (2012). "The continuing challenge of understanding and modeling hemodynamic variation in fMRI." *Neuroimage* **62**(2): 1017-1023.
- Laufs, H., A. Kleinschmidt, A. Beyerle, E. Eger, A. Salek-Haddadi, C. Preibisch and K. Krakow (2003). "EEG-correlated fMRI of human alpha activity." *Neuroimage* **19**(4): 1463-1476.
- Lindquist, M. A. and T. D. Wager (2007). "Validity and power in hemodynamic response modeling: a comparison study and a new approach." *Hum Brain Mapp* **28**(8): 764-784.
- Miezin, F. M., L. Maccotta, J. M. Ollinger, S. E. Petersen and R. L. Buckner (2000). "Characterizing the hemodynamic response: effects of presentation rate, sampling procedure, and the possibility of ordering brain activity based on relative timing." *Neuroimage* **11**(6 Pt 1): 735-759.
- Mo, J., Y. Liu, H. Huang and M. Ding (2013). "Coupling between visual alpha oscillations and default mode activity." *Neuroimage* **68**: 112-118.
- Petridou, N., C. C. Gaudes, I. L. Dryden, S. T. Francis and P. A. Gowland (2013). "Periods of rest in fMRI contain individual spontaneous events which are related to slowly fluctuating spontaneous activity." *Hum Brain Mapp* **34**(6): 1319-1329.
- Sampat, M. P., G. J. Whitman, T. W. Stephens, L. D. Broemeling, N. A. Heger, A. C. Bovik and M. K. Markey (2006). "The reliability of measuring physical characteristics of spiculated masses on mammography." *Br J Radiol* **79 Spec No 2**: S134-140.
- Shrout, P. E. and J. L. Fleiss (1979). "Intraclass correlations: uses in assessing rater reliability." *Psychological bulletin* **86**(2): 420.

Tagliazucchi, E., P. Balenzuela, D. Fraiman and D. R. Chialvo (2012). "Criticality in large-scale brain fMRI dynamics unveiled by a novel point process analysis." Front Physiol **3**: 15.

Wang, Z., G. K. Aguirre, H. Rao, J. Wang, M. A. Fernandez-Seara, A. R. Childress and J. A. Detre (2008). "Empirical optimization of ASL data analysis using an ASL data processing toolbox: ASLtbx." Magn Reson Imaging **26**(2): 261-269.

Webb, J. T., M. A. Ferguson, J. A. Nielsen and J. S. Anderson (2013). "BOLD Granger causality reflects vascular anatomy." PLoS One **8**(12): e84279.

Wu, G. R., W. Liao, S. Stramaglia, J. R. Ding, H. Chen and D. Marinazzo (2013). "A blind deconvolution approach to recover effective connectivity brain networks from resting state fMRI data." Med Image Anal **17**(3): 365-374.

Yeo, B. T., F. M. Krienen, J. Sepulcre, M. R. Sabuncu, D. Lashkari, M. Hollinshead, J. L. Roffman, J. W. Smoller, L. Zollei, J. R. Polimeni, B. Fischl, H. Liu and R. L. Buckner (2011). "The organization of the human cerebral cortex estimated by intrinsic functional connectivity." J Neurophysiol **106**(3): 1125-1165.